AGU PUBLICATIONS

JGR

Journal of Geophysical Research: Atmospheres

RESEARCH ARTICLE
10.1002/2014JD022479

**Key Points:**
- LULCC-induced climate changes show clear seasonality
- LULCC led to significant changes in climate variability
- The mechanisms of LULCC-induced changes in regional climate are elucidated

**Supporting Information:**
- Readme
- Tables S1–S4
- Figure S1
- Figure S2
- Figure S3
- Figure S4
- Figure S5
- Figure S6
- Figure S7
- Figure S8

**Correspondence to:**
C. Fu,
fcb@nju.edu.cn

**Citation:**
Xu, Z., R. Mahmood, Z.-L. Yang, C. Fu, and H. Su (2015), Investigating diurnal and seasonal climatic response to land use and land cover change over monsoon Asia with the Community Earth System Model, *J. Geophys. Res. Atmos.*, *120*, 1137–1152, doi:10.1002/2014JD022479.

Received 26 AUG 2014
Accepted 15 JAN 2015
Accepted article online 20 JAN 2015
Published online 12 FEB 2015



# Investigating diurnal and seasonal climatic response to land use and land cover change over monsoon Asia with the Community Earth System Model

**Zhongfeng Xu[1,2], Rezaul Mahmood[3], Zong-Liang Yang[1,4], Congbin Fu[5,2,1], and Hua Su[4]**

[1]RCE-TEA, Institute of Atmospheric Physics, Chinese Academy of Sciences, Beijing, China, [2]Jiangsu Collaborative Innovation Center for Climate Change, Nanjing University, Nanjing, China, [3]Department of Geography and Geology, Western Kentucky University, Bowling Green, Kentucky, USA, [4]Department of Geological Sciences, Jackson School of Geosciences, University of Texas at Austin, Austin, Texas, USA, [5]Institute for Climate and Global Change Research and School of Atmospheric Sciences, Nanjing University, Nanjing, China

**Abstract** Land use and land cover change (LULCC) is primarily characterized as forest conversion to cropland for the development of agriculture. Previous climate modeling studies have demonstrated the LULCC impacts on mean climate and its long-term trends. This study investigates the diurnal and seasonal climatic response to LULCC in monsoon Asia through two numerical experiments with potential and current vegetation cover using the fully coupled Community Earth System Model. Results show that LULCC leads to a reduced diurnal temperature range due to the enhanced (reduced) diurnal cycle of the ground heat flux (sensible heat flux). Daily minimum surface air temperature ($T_{min}$) exhibits a clear seasonality over India as it increases most in the premonsoon season and least during the summer monsoon season. Similarly, a strong anticyclonic anomaly is present at 850 hPa over India in spring and over eastern China in autumn, but weak changes in circulation appear in winter and summer. In addition, the LULCC results in significant changes in the variability of the 2 m air temperature, as characterized by an enhanced variability in India and a reduced variability in northern China to eastern Mongolia in autumn and winter. Possible land-atmosphere feedback loops involving surface albedo, soil moisture, evapotranspiration, atmospheric circulation, and precipitation are offered as biogeophysical mechanisms that are responsible for the region-specific LULCC-induced diurnal and seasonal response.

## 1. Introduction

Human activities have significantly altered land use and land cover primarily by transforming natural ecosystems into agricultural areas over the past centuries. The most significant land use and land cover change (LULCC) has occurred in East Asia, South Asia, Europe, and North America [*Ramankutty and Foley*, 1999]. The Intergovernmental Panel on Climate Change Fifth Assessment Report documents that the LULCC has led to a global radiative forcing of $-0.15 \pm 0.10\,\mathrm{W\,m^{-2}}$ since 1750 due to the increased surface albedo [*Myhre et al.*, 2013]. In addition to the radiative effect [*Eliseev and Mokhov*, 2011a], nonradiative forcing, such as changes in evapotranspiration, is also important, particularly at the regional scale [*Pitman et al.*, 2009; *Lawrence and Chase*, 2010]. Model simulations show that the impacts of LULCC on temperature and precipitation are less important than those of large-scale sea surface temperature (SST) anomalies at the global scale. However, in regions with significant LULCC, their impacts can be equal to or more than those caused by SST forcing [*Findell et al.*, 2009]. In addition to the mean climate, LULCC also strongly impacts temperature and rainfall extremes, which can amplify or mask the effect of increasing $CO_2$ [*Pitman et al.*, 2012; *Avila et al.*, 2012].

Monsoon Asia, which comprises South, Southeast, and East Asia, is a typical monsoon region with intense human activities. Approximately half of the world's population lives in monsoon Asia, where the land cover has been dramatically changed by human activities over the past centuries [*Ramankutty and Foley*, 1999; *Goldewijk*, 2001; *United Nations*, 2013]. Because of this reason, the potential impacts of LULCC on monsoon Asian climate have drawn more and more attention. Numerous studies have been performed using climate models in various subregions of monsoon Asia, such as the Tibetan Plateau [e.g., *Cui et al.*, 2006], north China [e.g., *Zhang*, 2004], northwest China [e.g., *Lv and Chen*, 1999; *Ding et al.*, 2005], south China [e.g., *Zheng et al.*,

2002a, 2002b], India [e.g., *Sud and Smith*, 1985; *Douglas et al*., 2006, 2009; *Sen Roy et al*., 2007, 2011], East Asia [*Zhang and Gao*, 2009], Southeast Asia [e.g., *Delire et al*., 2001], and Asia [*Takata et al*., 2009] over the recent decades. Different from these earlier studies, especially *Zhang and Gao* [2009] and *Takata et al*. [2009], our focus here is on the entire monsoon Asian region, using a significantly more sophisticated climate system model with a finer spatial resolution and with explicit ocean-atmosphere interactions. Many of previous modeling studies on the climatic effects of land cover change did not consider ocean-atmosphere interactions [e.g., *Fu*, 2003; *Findell et al*., 2009; *Pitman et al*., 2009; *Avila et al*., 2012; *Boisier et al*., 2012], but recent works suggest that the ocean-atmosphere coupling effect may modulate the magnitude of the climate response to LULCC [*Delire et al*., 2001; *Davin and de Noblet-Ducoudré*, 2010; *Ma et al*., 2012]. Using the National Center for Atmospheric Research (NCAR) Community Climate System Model (CCSM) with fully dynamic atmosphere, ocean, sea ice, and land surface (vegetation), *Notaro et al*. [2011] examined the response of global monsoons to an idealized reduction in the vegetation fraction. Their results show that the East Asian monsoon season occurs earlier in the year, while the change in the Indian monsoon is weak.

*Lawrence and Chase* [2010] simulated the impacts of LULCC on the global climate in terms of changes in temperature, precipitation, energy, and the hydrological budget over different regions using the CCSM version 3. In this study, we investigate the LULCC impacts on the monsoon Asian climate by generally following the experimental design of *Lawrence and Chase* [2010]. However, our simulations use the Community Earth System Model (CESM), which includes the updated representation of the land surface as the Community Land Model version 4 (CLM4). Compared to the earlier CLM3, which was used in CCSM3 in *Lawrence and Chase* [2010], CLM4 better simulates soil moisture dynamics, surface albedo, and soil temperature [*Lawrence et al*., 2011]. In addition, our analysis focuses on the diurnal and seasonal response of the monsoon Asian climate to LULCC, with an in-depth investigation of biogeophysical feedbacks involving land cover, soil moisture, surface albedo, soil temperature, and atmospheric circulation, an important topic that has not been thoroughly addressed in previous studies.

## 2. Methodology

### 2.1. Model Description

This study uses CESM version 1 [*Gent et al*., 2011]. CESM is a fully coupled Earth system model comprising four separate models that simultaneously simulate the Earth's atmosphere, ocean, land surface, and sea ice. The atmospheric model is the Community Atmosphere Model (CAM) with the Lin-Rood finite volume core [*Lin*, 2004] and 26 vertical layers. The horizontal grid resolution was set to $2.5° \times 1.875°$. The ocean component is the Parallel Ocean Program version 2 [*Smith et al*., 2010], which is a three-dimensional general ocean circulation model. The land surface model is the Community Land Model version 4 (CLM4), with 15 vertical levels for vegetated, wetland, and glacier land units and 10 vertical levels for lakes. CLM4 includes 15 plant functional types, as well as bare ground, lakes, and glaciers. Each vegetation type has its own leaf and stem areas, root distributions, optical properties, and canopy top and bottom heights [*Dai et al*., 2003]. CLM4 does not differentiate the types of crops. All types of crops are given the same parameters. CLM4 includes improved soil evaporation and snow parameterizations compared with its predecessor. These updates result in more realistic soil moisture dynamics, snow cover, soil temperature in organic-rich soils, and albedos in forests and grasslands [*Lawrence et al*., 2011]. The sea ice component is the Community Ice Code, which is a dynamic-thermodynamic model that includes a subgrid-scale ice thickness distribution [*Bitz et al*., 2001; *Lipscomb*, 2001].

CESM and its predecessors, the Community Climate System Model (CCSM), have been widely used to study the paleoclimate and climate of the recent past and to project future climate change. The fully coupled CCSM3 greatly improves South Asian monsoon rainfall relative to the atmosphere model (CAM3) due to the presence of thermodynamic air-sea coupling over the South Asia region [*Meehl et al*., 2006]. In comparison with CCSM3, CCSM4 produces more realistic simulations of soil water from one season to the next, which improves the simulation of the latent heat flux in the dry and transitional seasons [*Gent et al*., 2011]. The seasonality of LULCC-induced changes in the surface air temperature and land-atmosphere interactions are closely related to the precipitation and soil moisture climatology, which is elucidated in the next section. In addition, the intraseasonal and interannual variabilities in the Asia-Australian monsoon in CCSM4 are improved relative to CCSM3 [*Meehl et al*., 2012]. The improvements in the simulated

**Table 1.** LULCC-Induced Fractional Change in CLM Plant Functional Types (CurVeg-PotVeg) Over the Land Area in India (10–30°N, 70–90°E) and in Eastern China (20–50°N, 105–125°E)[a]

| PFT | India | Eastern China |
|---|---|---|
| Bare | −5.15 | −1.72 |
| Needleleaf evergreen temperate tree | −0.73 | −15.19 |
| Needleleaf evergreen boreal tree | 0.00 | −0.49 |
| Needleleaf deciduous boreal tree | 0.00 | 0.00 |
| Broadleaf evergreen tropical tree | −3.07 | −0.23 |
| Broadleaf evergreen temperate tree | −0.25 | −0.44 |
| Broadleaf deciduous tropical tree | −38.21 | −1.29 |
| Broadleaf deciduous temperate tree | −6.20 | −15.58 |
| Broadleaf deciduous boreal tree | 0.00 | −2.16 |
| Evergreen temperate shrub | 0.00 | 0.00 |
| Deciduous temperate shrub | −4.10 | −0.66 |
| Deciduous boreal shrub | 0.00 | −0.04 |
| C3 grass arctic | 0.00 | +0.02 |
| C3 grass nonarctic | −0.04 | +7.11 |
| C4 grass | +3.65 | +5.71 |
| Crop | +46.71 | +20.79 |
| Urban | +7.40 | +4.16 |

[a]Only the grid cells over land with surface pressure higher than 850 hPa were included in the statistics.

precipitation, soil water, and monsoon variabilities provide more confidence for investigating the impacts of LULCC on Asian climate using CESM.

### 2.2. Experimental Design

To examine the effect of large-scale LULCC on monsoon Asia climate, two experiments were conducted using the fully coupled CESM. The first experiment (PotVeg) was driven by potential vegetation cover data, and the second (CurVeg) was driven by current vegetation cover data. The potential vegetation distribution data were provided by *Lawrence and Chase* [2010] and were derived from the global land cover change data created by *Ramankutty and Foley* [1999]. In the CurVeg experiment, a remote sensing vegetation map valid in 2000 from Moderate Resolution Imaging Spectroradiometer data was used. In this study, the vegetation types and their fractional cover do not change with time; the leaf area index (LAI) varies monthly but not interannually. The soil color, soil texture, and areal percentages of lakes and glaciers in each grid cell are identical in all of the experiments. The ocean model was initialized from the present-day oceanic temperature and salinity conditions and from a state of rest. Both simulations were integrated for 100 years. Note that the deep ocean requires hundreds of years to reach an equilibrium state, but the upper ocean can reach equilibrium within a few decades. Investigating interannual variability requires the upper ocean be in a reasonable state of equilibrium [*Kantha and Clayson*, 2000]. In our simulations, the annual mean SST can reach equilibrium within 10–20 years in the western Pacific and northern Indian Oceans, which is generally consistent with previous studies [e.g., *Abe et al*., 2003; *Wohlfahrt et al*., 2004; *Kioth*, 2004]. Deep soil moisture takes approximately 30 years to reach equilibrium in eastern China and India (not shown). Therefore, the first 40 years of the simulations were discarded for spin-up purposes.

Table 1 shows the fractional changes in various plant functional types (PFTs) between the current and potential vegetation maps over India and eastern China. In India, the loss of natural PFTs is dominated by decreases in broadleaf deciduous tropical trees, and cropland increases by approximately 47%. In eastern China, the primary loss of natural PFTs is due to the losses of needleleaf evergreen temperate trees and broadleaf deciduous temperate trees by approximately 15%, respectively. Consequently, cropland increases by approximately 21%. These changes in PFTs are generally consistent with those in *Lawrence and Chase* [2010]. As a result of these PFTs' changes, LAI shows a remarkable decrease over eastern China, the Indo-China peninsula, and India (Figure 1). The decrease in LAI is greater in India than in eastern China throughout the year because a higher percentage of forest is converted into cropland in India than in China (Tables 1 and S1 in the supporting information). The needleleaf evergreen temperate trees have a smaller albedo than the broadleaf deciduous tropical trees. As a result, the LULCC leads to a larger increase in surface albedo in eastern China than in India (Table S2).

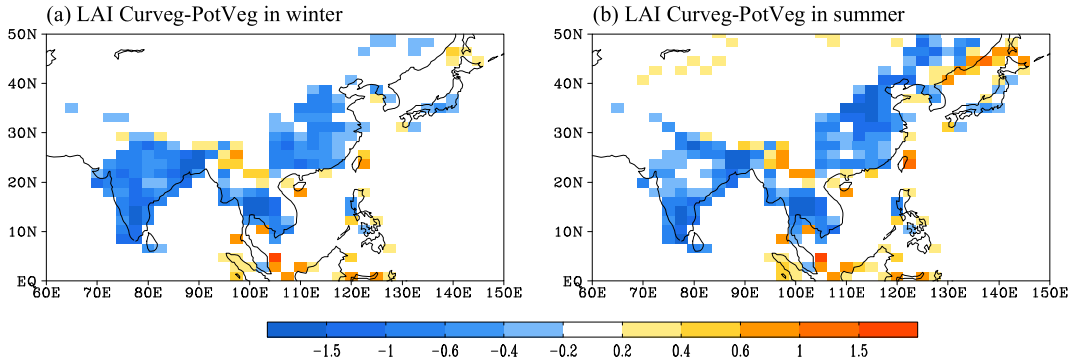


**Figure 1.** LULCC-induced changes (CurVeg-PotVeg) in leaf area index (LAI) in (a) winter (December-January-February) and (b) summer (June-July-August).

### 2.3. Data and Statistical Method

The National Centers for Environmental Prediction (NCEP)–National Center for Atmospheric Research (NCAR) reanalysis data [*Kalnay et al.*, 1996] and Climatic Research Unit (CRU) data [*Harris et al.*, 2014] were used to validate the performance of CESM in simulating monsoon Asian climate. The statistical significance of the difference in the time series between the CurVeg and PotVeg experiments was evaluated using the Student's *t* test, which takes the serial correlation into account [*Zwiers and von Storch*, 1995]. A field significance test [*Livezey and Chen*, 1983; *Elmore et al.*, 2006] was employed to evaluate the collective significance of the differences between two spatial distributions. The *F* test was employed to examine the significance of differences in the standard deviations between the CurVeg and PotVeg experiments.

## 3. Results

### 3.1. Evaluation of the Simulated Climate in Monsoon Asia

A 100 year modern day CESM simulation was produced, and the last 60 years were compared with observations or the NCEP-NCAR reanalysis data. CESM well reproduces the spatial patterns of sea level pressure and 850 hPa vector winds over monsoon Asia. A high-pressure system is centered over the Asian continent in winter, which is associated with northerly winds over East Asia and easterly winds over South Asia; a reversed pattern occurs in summer (Figure S1). In spring and autumn, the 850 hPa circulation is generally weaker than in winter and summer in both the NCEP-NCAR reanalysis and CESM simulations. CESM can reasonably simulate the Asian monsoon circulation and precipitation in a way similar to CCSM4 [*Meehl et al.*, 2012]. However, relative to the NCEP-NCAR reanalysis wind, CESM displays significant biases in monsoon circulation (Figure S1), as characterized by overestimated 850 hPa wind speeds over monsoon Asia in winter, spring, and autumn.

Similar to its predecessors, CESM does a fairly good job in reproducing the annual cycle of precipitation in monsoon Asia and the timing of the monsoon onset [*Meehl et al.*, 2006; *Notaro et al.*, 2011; *Lee et al.*, 2013], but significant precipitation biases are noted. For example, in comparison with CRU data, the simulated precipitation is underestimated by 0.02 mm $d^{-1}$ (2.5%) over eastern China in winter but is overestimated by 1.33, 0.95, and 0.75 mm $d^{-1}$ (41%, 20%, and 38%) in spring, summer, autumn, respectively. Over India, the precipitation is overestimated by 0.01, 2.00, 1.64, and 0.55 mm $d^{-1}$ (2.3%, 35%, 74%, and 56%) in spring, summer, autumn, and winter, respectively. CESM captures the annual cycle of $T_{max}$, $T_{min}$, and diurnal temperature range (DTR) over both India and eastern China (Figure S2). However, the simulated $T_{max}$ is lower than CRU data by about 2°C throughout the year, and the simulated $T_{min}$ is significantly higher than CRU by 2–4°C in India throughout the year (Figure S2c). As a result, DTR is underestimated by 1–4°C in India (Figure S2e). In eastern China, the simulated $T_{min}$ is significantly higher than CRU data by 2–3°C from April to September but is lower by 1–2°C in winter (Figure S2d). The errors in the DTR are generally smaller in eastern China than in India (Figures S2e and S2f).

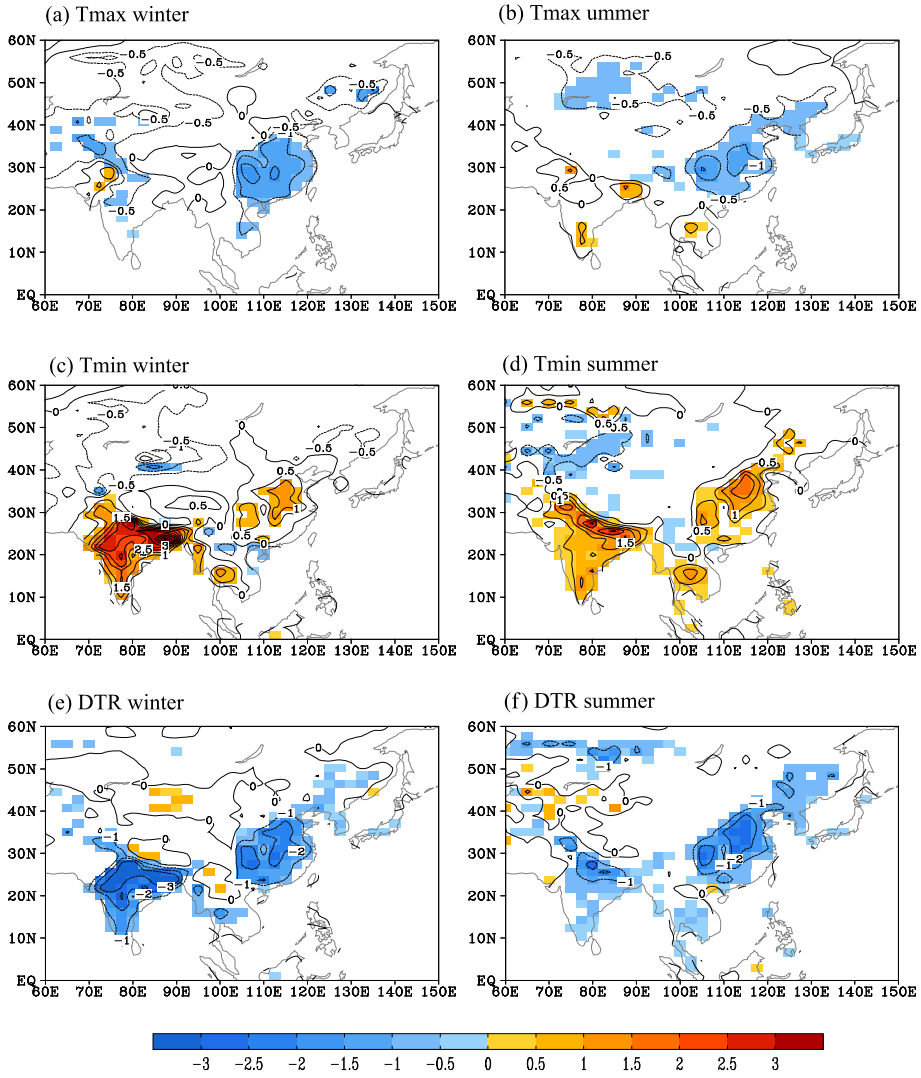


**Figure 2.** Difference in the 2 m air temperature (°C) between the CurVeg and PotVeg experiments in (a, c, and e) winter (December-January-February) and (b, d and f) summer (June-July-August). $T_{max}$: daily maximum temperature, $T_{min}$: daily minimum temperature, and DTR: diurnal temperature range (°C). The shaded areas denote the significance level of 0.05. All changes in $T_{max}$, $T_{min}$, and DTR have a field significance level of 0.05.

### 3.2. Diurnal and Seasonal Climatic Response to LULCC

#### 3.2.1. Surface Air Temperature

LULCC leads to a significant decrease in $T_{max}$ by 1–1.5°C in eastern China in both winter and summer (Figures 2a and 2b). A weak decrease (increase) in $T_{max}$ is found in India in winter (summer) (Figures 2a and 2b). In contrast, $T_{min}$ is significantly increased by 0.5–1°C (0.5–1.5°C) in eastern China and 0.5–3°C (0.5–2°C) in India in winter (summer) (Figures 2c and 2d). The magnitude of the change in the daily mean air temperature is similar to that in $T_{max}$ and $T_{min}$ but closer to that in $T_{min}$ (not shown), suggesting that the nighttime temperature increase plays a more important role than the daytime temperature decrease in determining the change in the daily mean air temperature. A significant decrease in the DTR is found over India and eastern China in both seasons due to the significant increase in $T_{min}$ and the decrease (or weak increase) in $T_{max}$. The changes in $T_{min}$ and DTR are larger over India in winter than in summer (Figures 2c–2f).

To examine the time dependence of LULCC-induced changes in the surface climate, the annual cycle of the changes in $T_{max}$, $T_{min}$, T2m, and DTR over India and eastern China were assessed. In India, the LULCC-induced change in $T_{max}$ is weak throughout the year (Figure 3a). However, the LULCC leads to a significant increase in

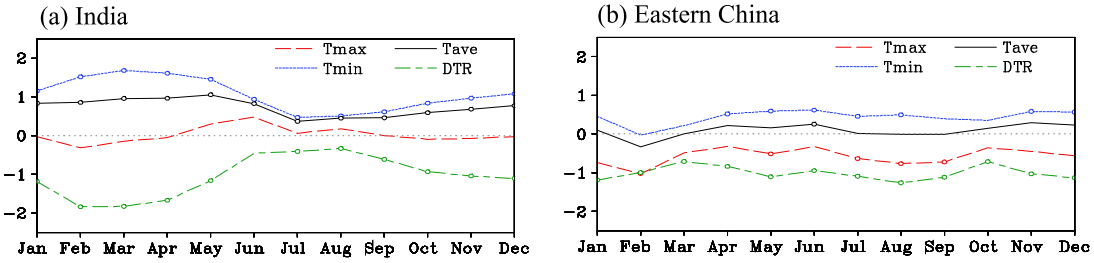


**Figure 3.** Annual cycle of the LULCC-induced (CurVeg-PotVeg) change in the daily maximum and minimum 2 m air temperature (°C), daily mean temperature, and DTR over the land grid cells (a) in India (10–30°N, 70–90°E) and (b) in eastern China (22–40°N, 105–120°E). Only the grid cells over land with surface pressures higher than 850 hPa were included in the statistics. The open circles indicate differences that reach the significance level of 0.05.

$T_{min}$ throughout the year. The change in $T_{min}$ shows a clear seasonality characterized by significant warming (1.5°C) in spring and a smaller warming (0.5°C) in summer. The annual cycle of the daily mean T2m basically follows that of $T_{min}$ except that the change is smaller. The maximum decrease in the DTR (−1.7°C) appears in February-March-April and the minimum decrease (−0.4°C) during the Indian summer monsoon season (Figure 3a). In eastern China, the LULCC results in a significant cooling in $T_{max}$ and a significant warming in $T_{min}$ throughout the year. The DTR is reduced by approximately 1°C throughout the year without a clear seasonality (Figure 3b). *Kalnay and Cai* [2003] also found that LULCC could lead to a decrease in the DTR when contrasting reanalysis data with observation data.

To investigate the causes of the LULCC-induced changes in the surface air temperature and its seasonality, we computed all components of the land surface energy balance equation using the three-hourly output from the PotVeg and CurVeg experiments:

$$R_a - \left(L_\uparrow - L_\downarrow\right) - H - \lambda E - G = 0 \tag{1}$$

The longwave radiation emitted from the land surface can be written as follows:

$$\sigma T^4 = R_a + L_\downarrow - H - \lambda E - G \tag{2}$$

where $\sigma$ is the Stefan-Boltzmann constant ($5.67 \times 10^{-8}\,\mathrm{W\,m^{-2}\,K^{-4}}$), $T$ is the land surface temperature (radiative temperature), $R_a$ is the absorbed solar radiation at the land surface (ASR), $L_\uparrow$ is the upward longwave radiation from the surface, $L_\downarrow$ is the downward atmospheric longwave radiation (ALR), $H$ is the sensible heat flux (SH), $\lambda E$ is the latent heat flux (LH), and $G$ is the ground heat flux (GHF). Subsequently, we can determine which component(s) of the energy budget is responsible for the change in the land surface temperature by analyzing changes in the land surface fluxes. A similar approach was employed in *Boisier et al.* [2012] to attribute changes in the monthly surface air temperature in North America and western Eurasia to changes in the surface energy budget components.

The climatology of land surface fluxes simulated by CESM is important to understand the impact of LULCC on regional climate. We briefly introduce the climatology of the land surface fluxes before analyzing the LULCC-induced changes. The climatological GHF exhibits a clear diurnal cycle characterized by a downward heat flux (positive) in the day and an upward heat flux (negative) at night throughout the year (not shown). The downward GHF transfers energy from the land surface into deeper soil, which decreases the land surface temperature in the day. The upward GHF transfers energy from deeper soil to the land surface and increases the land surface temperature at night. The sensible heat flux also shows a similar diurnal cycle but with an upward (positive) flux during the day and a downward (negative) flux at night (not shown). The positive (negative) SH transfers energy from the land surface (atmosphere) to the atmosphere (land surface), which then cools (warms) the land surface and warms (cools) the atmosphere. We only discuss the climatology of GHF and SH because they are the most important variables regarding the changes in diurnal cycle of surface air temperature based on the following analysis.

The LULCC-induced changes in GHF, SH, LH, ASR, ALR, and their sum over India and eastern China were assessed. The GHF, SH, and LH were multiplied by −1, respectively, for convenient comparison. Thus, a positive

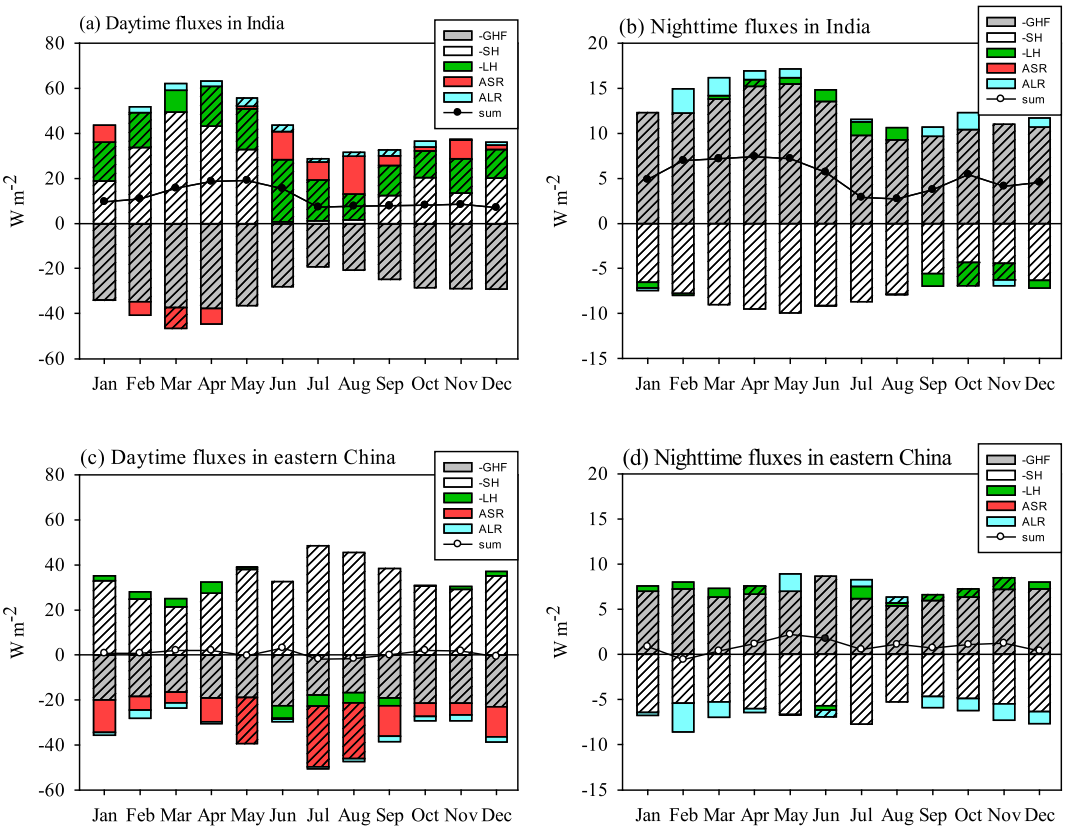


**Figure 4.** Annual cycle of the changes (CurVeg-PotVeg) in the daytime and nighttime fluxes (W $m^{-2}$) (a, b) in India (10–30°N, 70–90°E) and (c, d) in eastern China (20–40°N, 105–125°E). Only the grid cells over land with surface pressures higher than 850 hPa were included in the statistics. GHF: ground heat flux, SH: sensible heat flux, LH: latent heat flux, ASR: absorbed solar radiation at the land surface, ALR: atmospheric longwave radiation, and sum: sum of the five variables. The GHF, SH, and LH were multiplied by −1, respectively, for convenient comparison. A positive (negative) change warms up (cools) the land surface. The stippled bars indicate differences that reach the significance level of 0.05. Daytime (nighttime): UTC 09 (UTC 21) for India and UTC 06 (UTC 18) for eastern China.

(negative) change in the sum of the five variables warms (cools) the land surface based on equation (2). The sum of GHF, SH, LH, ASR, and ALR for both the day and night is positive, indicating a warming of the land surface over India (Figures 4a and 4b). The daytime land surface warming favors an increase in $T_{max}$ at 2 m. However, the LULCC-induced decrease in SH (Figure 4a) reduces the energy transfer from the land surface to the atmosphere, thereby reducing $T_{max}$. As a result, no significant change is found in $T_{max}$ over India (Figure 3a). In eastern China, no significant change is found in land surface temperature; thus, the weakening of SH accounts for the decrease in $T_{max}$ (cooling) throughout the year (Figures 3b and 4c). At night, the sum of GHF, SH, LH, ASR, and ALR is also positive, indicating a land surface warming in eastern China (Figure 4d). In addition, the weakening of the downward sensible heat flux helps maintain the nighttime air temperature and cools the land surface. As a result, $T_{min}$ significantly increases over India and eastern China throughout the year (Figures 3a, 3b, 4b, and 4d). Clearly, the LULCC-induced subdaily changes in the GHF and SH are significant in both India and eastern China throughout the year and are the primary factors leading to a significant decrease in DTR.

Interestingly, the most significant increase in $T_{min}$ over India occurs before the summer monsoon season, with a smaller increase during the summer monsoon season (Figure 3a). A similar seasonality of T2m is also found over western Eurasia, as characterized by the most significant decrease in T2m in spring [*de Noblet-Ducoudré et al.*, 2012]. The LULCC leads to an enhanced diurnal cycle of GHF, suggesting that more energy enters deeper soil during the day throughout the year. The energy transmitted to and absorbed by the deeper soils during the day is transferred toward the surface at night, leading to an increased nighttime surface temperature and a reduced DTR [cf. *Oke*, 1987; *Rosenberg et al.*, 1983]. On the other hand, the LULCC leads to a decrease in the

surface roughness length, which enhances the aerodynamic resistance. Consequently, the sensible heat flux shows a weakened diurnal cycle. The reduced downward SH from the atmosphere to the land surface at night is also favorable for maintaining the air temperature. Clearly, the maximum change in GHF and SH appears in spring and accounts for the most significant increase in $T_{min}$ over India in spring (Figures 3a and 4b). The maximum change in GHF is related to the highest absorbed solar insolation and the driest soil condition in spring (Figure S3). These conditions cause stronger and more effective heat transfer between the land surface and deeper soils, thereby increasing the downward GHF during the day and the upward GHF at night. Previous studies also suggest that drier soil and degradation of vegetation can lead to a reduction in DTR across North Africa and global monsoon regions [*Zhou et al*., 2007; *Notaro et al*., 2011]. A recent study using observed ground heat flux and radiation data from the Ecosystem Research Network developed by the Chinese Academy of Sciences suggests that the GHF is positively (negatively) correlated with net radiation (soil heat capacity) at the subdaily timescale [*Li et al*., 2012], which are consistent with our results. *Yang et al*. [1999] investigated the influence of vegetation on ground heat flux by using two land surface models; their study suggested that vegetation dampens the solar radiation at the surface and reduces the amplitude of the diurnal cycle of temperature, which in turn reduces the amplitude of the ground heat flux, and vice versa. LULCC is primarily characterized by a degradation of vegetation, which typically enhances the diurnal cycle of the GHF. The enhanced GHF and reduced SH plays a dominant role in determining T2m at the subdaily time scale in both India and eastern China. However, on the daily mean or longer time scales, the change in the daytime GHF (SH) is partly canceled out by the change in the nighttime GHF (SH). In this case, the changes in other land surface fluxes, such as LH, become important [*Lawrence and Chase*, 2010].

#### 3.2.2. Frequency Distribution of Daily 2 m Air Temperature

To examine the features of daily air temperature in response to the LULCC, the frequency of the daily air temperature anomalies in various temperature bins was computed (Figures S4 and S5). In India, the frequency distribution of $T_{min}$ is shifted to warmer conditions by roughly 2°C in spring and winter and less than 1°C in summer and autumn, suggesting the LULCC leads to more warm nights and less cold nights throughout the year. In contrast, the frequency of the daily $T_{max}$ shows either no clear change or a slight shift to the cooler conditions throughout the year. The change in the frequency of $T_{min}$ is related to the changes in the GHF and SH. The frequency of the nighttime GHF shows a clear shift to negative values in all seasons, indicating that the LULCC induces more strong GHF events and less weak GHF events at night, i.e., favoring a shift in $T_{min}$ toward warmer conditions (not shown). The frequency of the nighttime SH exhibits a positive shift, which is also favorable for the increase in the warmer $T_{min}$ events (not shown).

In eastern China, the change in the frequency distribution of the surface air temperature is generally much weaker than that in India (Figures S4 and S5). The frequency distribution of $T_{max}$ ($T_{min}$) shifts to colder (warmer) conditions throughout the year, indicating that the LULCC leads to more cold days and warm nights (Figure S5). The change in the frequency distribution of $T_{max}$ is clearer than that of $T_{min}$ in eastern China, in contrast to that in India. The cold shift in $T_{max}$ is stronger in summer and winter than in spring and autumn in eastern China. The frequency distributions of the GHF and SH are similar to those in India, which result in a shift in $T_{min}$ to the warmer conditions (not shown). However, the warm shift in $T_{min}$ is weaker in eastern China than in India because the LULCC leads to a larger increase in the land surface albedo in eastern China than in India (Table S2). The higher land surface albedo leads to lower daytime land surface temperatures, which partly negates the increase in the GHF and the nighttime land surface temperature. Meanwhile, the enhanced land surface albedo is favorable for the cold shift in the $T_{max}$ distribution.

#### 3.2.3. Precipitation and Circulation

LULCC leads to a decrease in precipitation over northern India throughout the year with a maximum decrease of 1 mm $d^{-1}$ in August (Figure S6). In terms of the percentage change in precipitation, the maximum decrease (30%) occurs over northern India in spring. However, the changes in precipitation do not reach the field significance level of 0.05. The LULCC causes an air temperature increase of 0.2–0.4°C from the surface to 850 hPa and a decrease of 0.2–0.4°C between 700 hPa and 200 hPa over India (not shown). The difference between the CurVeg and PotVeg experiments shows a clear anticyclonic circulation anomaly at 850 hPa over India in spring (Figure 5b); the circulation anomaly is associated with a tropospheric anomalous subsidence, which suppresses precipitation (Figures 6a and S6c). For the vertical circulation and precipitation, similar responses to the reduced vegetation are also found in autumn by *Notaro et al*. [2011]. The anticyclonic and subsidence anomalies are likely related to the LULCC-induced increase in the surface albedo (Table S2) and

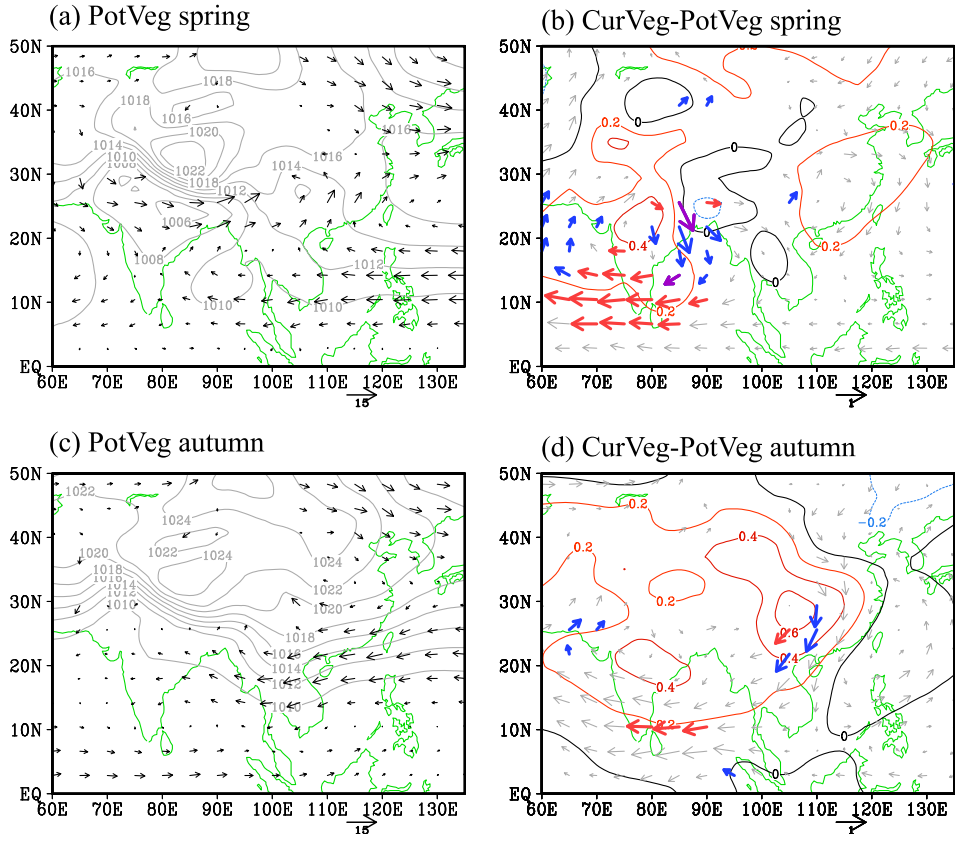


**Figure 5.** Climatological 850 hPa wind vectors (m $s^{-1}$) and sea level pressure (hPa) for the PotVeg experiment in (a) spring and (c) autumn. The difference in the 850 hPa wind vectors and sea level pressure between the CurVeg and the PotVeg experiments in (b) spring and (d) autumn. The red, blue, and purple arrows denote the changes in the zonal wind, meridional wind, and both of them that reach the significance level of 0.05, respectively. The changes in the zonal and meridional winds did not reach the field significance level of 0.05 in either season.

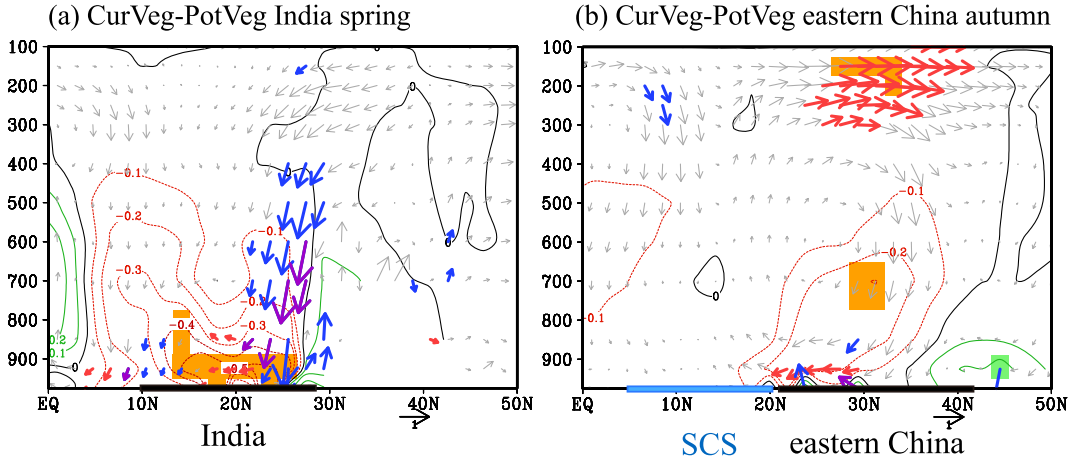


**Figure 6.** Difference in the meridional-vertical circulation and specific humidity (in g $kg^{-1}$) between the CurVeg and PotVeg experiments averaged over the (a) Indian region (70–90°E) in spring and (b) eastern China (105°–125°E) in autumn. The vertical velocity (in Pa $s^{-1}$) was multiplied by 100. The shaded area denotes that the difference in the specific humidity reached the significance level of 0.05. The blue, red, and purple arrows indicate the differences in vertical velocity, meridional wind, and both of them that reached the significance level of 0.05. The changes in vertical velocity in spring had a field significance level of 0.05. The changes in the other variables did not reach the field significance level of 0.05. The unit of the *y* axis is hectopascal.

decrease in the land surface roughness length and evapotranspiration over India. The enhanced surface albedo helps reduce the tropospheric air temperature by reducing both the longwave radiation emitted from the land surface and the sensible heat flux due to the lower land surface temperature. The reduced roughness weakens the sensible heat flux transfer from the land surface to the atmosphere, which also reduces the atmospheric temperature. The decrease in the surface roughness length reduces convergence and causes anomalous subsidence. Meanwhile, the decrease in evapotranspiration and roughness reduces the moisture flux from the land surface to the atmosphere and lowers the moisture content in the atmosphere (Figure 6a). The decrease in the moisture content helps further cool the atmosphere. In turn, the temperature decrease enhances the anomalous subsidence and leads to a decrease in the moisture content and precipitation (Figures 6 and S6). This positive feedback of temperature-subsidence-moisture likely plays an important role in enhancing the anomalous subsidence over India. Meanwhile, the decrease in the precipitation leads to a drier soil, which increases the land surface albedo and reduces evapotranspiration. The positive feedback of precipitation-soil moisture-evaporation also enhances the impact of LULCC on the regional climate. These atmospheric responses to LULCC are more obvious in spring and autumn when advection is weaker than in the summer and winter monsoon seasons (Figures 5 and S7).

In eastern China, the most significant change in the lower tropospheric circulation appears in autumn, as characterized by an anomalous northerly wind (Figure 5d). LULCC leads to a significant air temperature decrease of 0.2–0.4°C from the surface to 200 hPa over eastern China (not shown). A significant southerly wind anomaly is simulated above 300 hPa, with an anomalous descending and ascending motions at approximately 35°N and 20°N, respectively. A negative moisture anomaly is found over eastern China in association with the anomalous subsidence over 35°N and the northerly wind in the lower troposphere (Figure 6b). A negative anomaly in the tropospheric air temperature is also found between 20°N and 35°N (not shown). The anomalous circulation over eastern China in autumn likely results from the same mechanism responsible for the anomalous circulation in India in spring. Specifically, the LULCC-induced decreases in roughness and evapotranspiration reduce the sensible heat flux and moisture flux from the land surface to the atmosphere, which leads to a decrease in the tropospheric air temperature and moisture. The reduced atmospheric moisture further cools the air due to the decrease in the longwave radiation absorbed by the water vapor. The decrease in the air temperature enhances the subsidence, which leads to a northerly anomaly in the lower troposphere. The enhanced northerly wind is favorable for triggering convection when it flows over the warm sea surface of the South China Sea [e.g., *Chang and Lau*, 1980]. The enhanced ascent flows northward in the upper troposphere (Figure 6b). Similar to the circulation anomaly over India in spring, the most significant circulation anomaly induced by LULCC appears in the region with weak climatological wind speeds over eastern China (Figures 5 and S7). Therefore, the weak background circulation is favorable for maintaining the influence of LULCC on the regional climate. In contrast, eastern China and India are dominated by strong monsoon circulations during winter and summer that suppress the LULCC-induced changes in the regional land-atmospheric fluxes and circulations. However, the LULCC-induced surface albedo change likely plays a more important role in eastern China than in India because the change in the surface albedo is much greater in eastern China than in India in autumn (Table S2). However, the LULCC-induced LAI change is larger in India than in eastern China (Table S1). As a result, LULCC leads to a more significant decrease in LH in India but a more distinct decrease in ASR in eastern China (Figures 4a and 4c). Therefore, in terms of the seasonal mean climate response to LULCC, the thermal response is more important in eastern China while the hydrologic response is more crucial in India. These are generally consistent with the findings in *Notaro et al.* [2011].

Some changes in the lower tropospheric circulation can also be found during the summer and winter monsoon seasons, although the response in the atmospheric circulation is weaker than that in spring and autumn. LULCC enhances the East Asian winter monsoon, as characterized by the stronger 850 hPa northerly flow, and weakens the East Asian summer monsoon, as characterized by the weaker southerly flow over eastern China (Figure S7). The response of the Asian winter and summer monsoon circulations to LULCC as simulated by the fully coupled CESM is qualitatively consistent with previous studies that used regional climate models or global circulation models [e.g., *Fu*, 2003; *Gao et al*., 2003; *Chen et al*., 2006]. Note that our study may have underestimated the influence of LULCC on the East Asian winter and summer monsoon circulations because CESM overestimates the East Asian monsoon intensity (Figure S1), which typically suppresses the influence of LULCC on the regional circulation as we discussed previously.

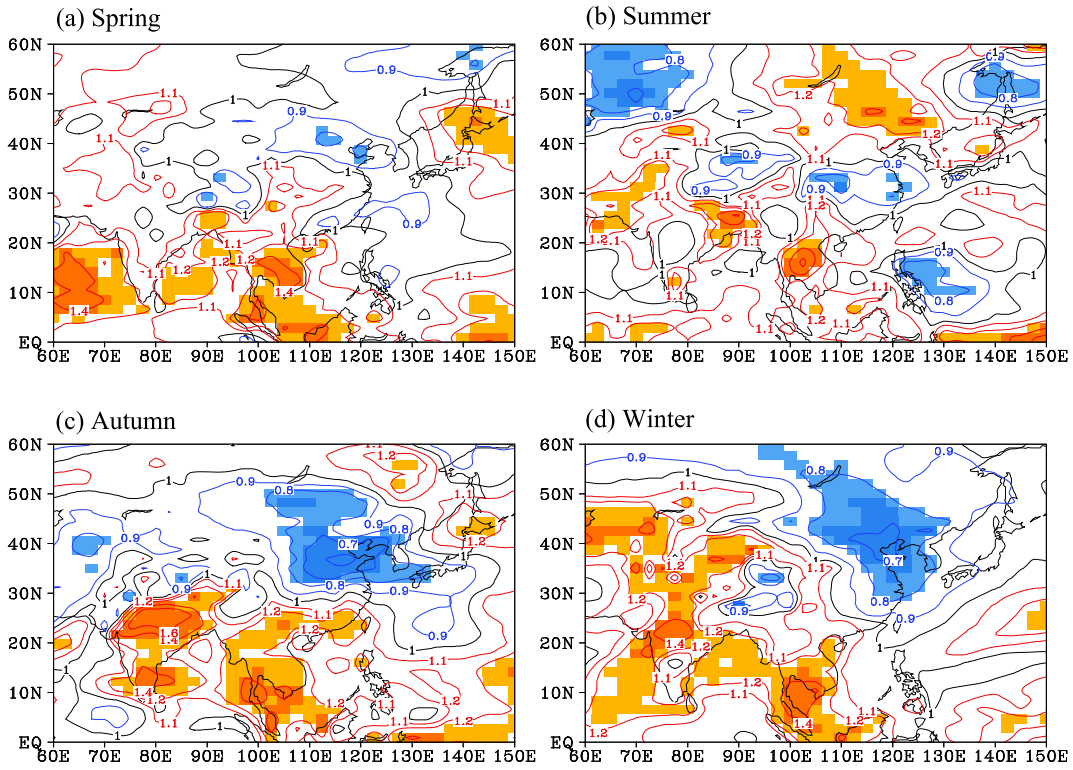


**Figure 7.** (a–d) LULCC-induced changes in the standard deviation of the seasonal surface air temperature measured by the ratio of the standard deviation simulated by the CurVeg to the PotVeg experiment. The standard deviations were computed from seasonal anomalies of T2m. The dark (shallow) shaded area denotes that the difference reaches the significance level of 0.01 (0.05). *F* tests were employed to examine the significance of the changes in the standard deviation.

### 3.3. Climate Variability

In this section, we examined the LULCC-induced changes in the temperature variability. The standard deviation of the monthly T2m (SDT) measures the magnitude of the temperature variability. Over the Asian monsoon region, the LULCC-induced change in SDT is larger in autumn and winter than in spring and summer, as characterized by a significant decrease in the SDT in the north China–east Mongolia (NCEM) region and a significant increase in the SDT in India in autumn and winter (Figure 7). Across the Indo-China peninsula, the SDT significantly increases throughout the year. In this section, we specifically focused on the most significant changes in the T2m variability over India and over the NCEM region in autumn and winter. To investigate the mechanism of the changes in the T2m variability, we need to determine how T2m is coupled with other variable. To do so, we computed the correlation coefficients of T2m with a number of variables. Then, we selected the variables which closely correlated with the T2m. Meanwhile, the standard deviation of the selected variables should show the same change in sign as the SDT. Lastly, we explained how these selected variables coupled with the T2m based on physical laws.

Climate variability can be strongly modulated by land-atmosphere interaction [*Seneviratne et al.*, 2006]. Semiarid regions generally show the strongest land-atmosphere coupling strength [*Koster et al.*, 2004, 2006]. To determine why the autumn SDT exhibits a significant increase in India, the climatological mean soil moisture and its changes induced by the LULCC were analyzed (Figure S8). In autumn, northwestern India is a transition zone between dry and wet climates. In this region, T2m is negatively correlated with soil water in the top 10 cm of the soil (SW10) and evapotranspiration, with correlation coefficients of −0.7 and −0.6, respectively. Thus, soil moisture likely controls evapotranspiration and temperature. Over the other regions of India, T2m is significantly and positively correlated with SW10, indicating a strong atmospheric control over evapotranspiration [*Seneviratne et al.*, 2010]. LULCC leads to a significant decrease in SW10, which is associated with decreased precipitation over northern India (Figures S6 and S8). As a result, the dry-to-wet transition zone shifts eastward. Meanwhile, the region with a negative correlation between T2m and SW10 also

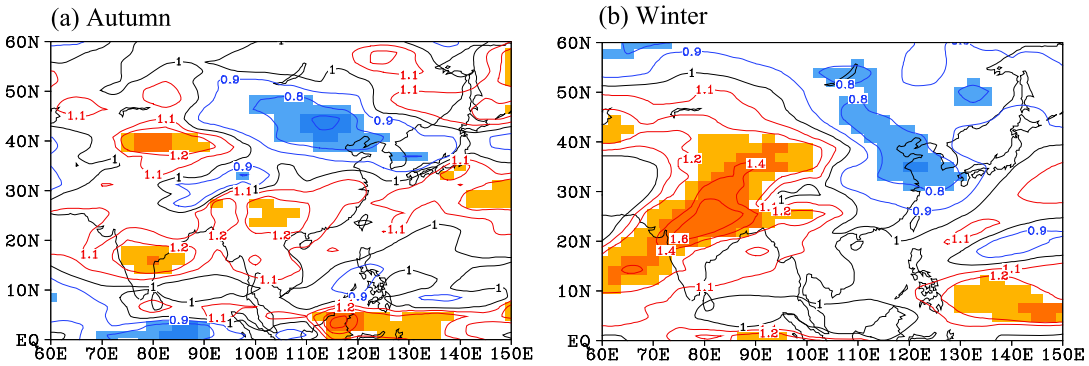


**Figure 8.** As in Figure 7 but for the vertically integrated precipitable water. The shallow (dark) shaded area denotes that the difference reaches the significance level of 0.05 (0.01).

extends eastward and enhances the T2m variability over northern India due to the increased land-atmosphere coupling strength (not shown). Meanwhile, similar to the T2m, SW10 also shows a significantly increased variability over India, which is favorable for enhancing T2m variability (not shown).

In winter, a significant increase in the T2m variability is also found in northern India (Figure 7d). However, the change is weaker than that in autumn. As in autumn, LULCC leads to a decrease in the climatological mean SW10 in winter (Figures S8c and S8d). However, there is no clear change in the standard deviation of SW10 (not shown). Moreover, the correlation between SW10 (LH) and the land surface temperature is rather weak, indicating that there is no coupling between SW10 and the land surface temperature in winter (not shown). Thus, the change in the T2m variability should not link to the change in SW10 variability in India in winter. Instead, T2m is closely linked to the vertically integrated precipitable water (VIPW), with correlation coefficients ranging from 0.4 to 0.7 for both the PotVeg and CurVeg experiments. Meanwhile, similar to T2m, VIPW shows significantly enhanced variability over northern India (Figures 7d and 8d). An increase in VIPW leads to more downward longwave radiation and land surface warming due to the greenhouse effect of water vapor. The increased land surface temperature is favorable for increasing precipitable water given the control of air temperature on water holding capacity of the atmosphere. Thus, the increase in the T2m variability is likely the result of a positive feedback of VIPW-atmospheric longwave radiation (ALR)-air temperature in India in winter. LULCC leads to a reduced soil heat capacity due to the decrease in soil moisture (Figure S8d). Thus, the response of land surface temperature should be more sensitive to the change in ALR in CurVeg than in PotVeg. As a result, the positive feedback of VIPW-atmospheric longwave radiation (ALR)-air temperature and T2m variability is stronger in CurVeg relative to that in PotVeg.

Similar to the LULCC-induced changes in the 850 hPa circulation, the LULCC-induced change in the T2m variability in India in winter is also strongly affected by the strength of background circulation. A weak background circulation leads to a stronger T2m variability. Specifically, the ratio of SDT in the CurVeg to that in the PotVeg is 1.4–1.6 (1.1–1.2) when the 850 hPa wind speeds averaged over South Asia (10–25°N, 60–100°E) are smaller (larger) than its climatological mean in winter. In this circumstance, how is the weak T2m variability in India in spring (Figure 7a) explained since the climatological mean wind speed is much weaker in spring than that in winter? The weak T2m variability could result from a negative feedback of VIPW/cloud fraction–land surface temperature in spring. The increase in VIPW/cloud fraction leads to less downward solar radiation at the land surface and lower air temperature. The decrease in air temperature is favorable for decreasing VIPW. The change in VIPW/cloud fraction strongly influences the shortwave radiation rather than the longwave radiation in spring due to the maximum downward solar radiation at land surface in the year. As a result, the negative feedback occurs in spring.

In the NCEM region, T2m exhibits significantly reduced interannual variability in both autumn and winter (Figures 7c and 7d). In autumn, T2m is significantly correlated with ALR, the snow fraction (FSNO), and VIPW, suggesting that T2m is likely coupled with these variables (Table S3). Among these variables, VIPW exhibits the most significantly reduced variability in the NCEM region (Table S4). The region with reduced VIPW variability is roughly coincided with the reduced T2m variability (Figures 7c and 8a). A decrease in VIPW

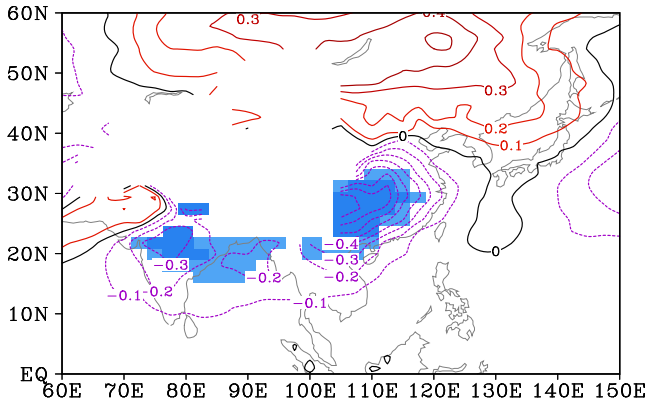


**Figure 9.** LULCC-induced changes (CurVeg-PotVeg) in the climatological mean 850 hPa air temperature in autumn. The shallow (dark) shaded area denotes differences that reach the significance level of 0.05(0.01). The changes in the air temperature did not reach the field significance level of 0.05.

causes a reduction in the downward longwave radiation, which results in a decrease in the land surface temperature, and vice versa. Thus, the reduction of the T2m variability is likely related to the changes in the VIPW variability through the greenhouse effect of water vapor. In addition, temperature advection likely plays a more important role in the decrease of T2m variability over the NCEM region in autumn. As shown in Figure 9, there is a remarkable decrease in the 850 hPa temperature over eastern China along 30°N and an increase in the 850 hPa temperature over Siberia along 50°N. The temperature gradient anomaly is the opposite of the climatological mean temperature gradient. Hence, LULCC leads to a decrease in the climatological mean meridional temperature gradient between 30°N and 50°N, where T2m also exhibits a significantly reduced variability. In association with the decrease in the meridional temperature gradient, cold advections associated with northerly anomalies and warm advections associated with southerly anomalies are reduced; in turn, the variability in 850 hPa air temperature decreases. Note that the region with the reduced meridional air temperature gradient exhibits reduced air temperature variability from the surface to 300 hPa over East Asia (figures not shown). This result implies that the meridional temperature advection plays an important role in the interannual variability of the air temperature in the NCEM region in autumn.

In winter, the LULCC causes an overall cooling without a clear change in the temperature gradient. As a result, the meridional temperature advection does not impact the temperature variability over the NCEM region in winter. As shown in Table S3, T2m is significantly correlated with ALR, SH, LH, FSNO, and VIPW. Among the factors, ALR, LH, and VIPW show distinct reduced variabilities (Table S4). In addition, the correlation coefficient between VIPW and T2m is generally higher than 0.8 in East Asia north of 40°N; thus, the T2m variability is likely dominated by the VIPW variability. The spatial pattern of the VIPW variability is very similar to that of the T2m variability (Figures 7d and 8b). The correlation coefficient between Figures 7d and 8b is 0.63. These values suggest that the T2m variability is likely driven by the VIPW variability in East Asia in winter. An increase in the VIPW leads to enhanced downward longwave radiation, which results in a higher land surface temperature, more snow melting, more LH, lower snow fraction, and vice versa (Table S3).

## 4. Discussion and Conclusions

Two experiments using potential and current vegetation cover were conducted with the fully coupled CESM to investigate the influence of LULCC on the seasonality of monsoon Asia climate. Specifically, we focused on the diurnal temperature range, annual temperature cycle, monsoon circulation and precipitation, and temperature variability. LULCC leads to a significant decrease in the DTR in eastern China due to the decrease in $T_{max}$ and increase in $T_{min}$ throughout the year. In India, the change in the DTR shows a strong seasonality characterized by a decrease of 1.7°C in spring, 0.4°C in summer, and 1°C in the other seasons. The decrease in the DTR is primarily due to the enhanced diurnal cycle of the GHF and the weakened diurnal cycle of SH. The maximum change in the GHF occurs in spring when the land surface absorbs the highest solar radiation and when the soil is driest; as a result, the maximum decrease in the DTR occurs in spring. Historical records indicated that $T_{min}$ experiences a larger increase than $T_{max}$ over East Asia, a large part of Europe, and North America [*Karl et al.*, 1993; *Easterling et al.*, 1997; *Shiu et al.*, 2009; *Li and Wang*, 2012]; therefore, the DTR decreases. Some climate model simulations indicate that higher greenhouse gas concentrations result in a decrease in the DTR by approximately 0.2°C per century, which is much smaller than the observed change [e.g., *Stone and Weaver*, 2002; *Zhou et al.*, 2010]. Our study suggest that LULCC,

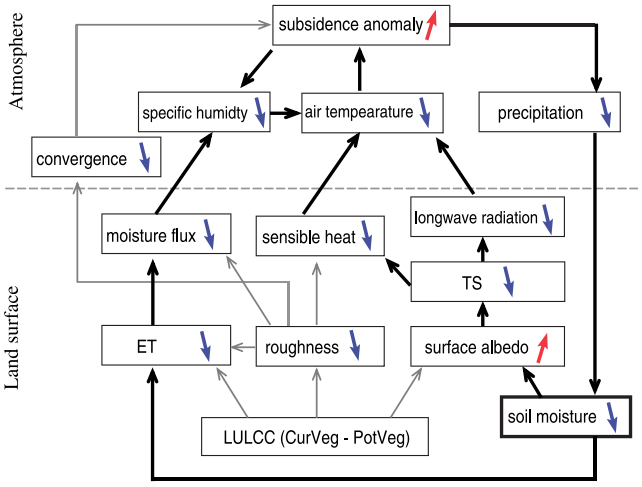


**Figure 10.** Schematic chart of the influence of LULCC on land surface fluxes and atmospheric circulation in Asia. The positive feedback loops are shown using thicker and darker arrows.

in addition to the greenhouse gas and aerosol [*Zhou et al*., 2010], has a substantial influence on the decrease in the DTR. Note that our study does not consider irrigation process, which may further enhance the impact of LULCC on DTR [*Mahmood et al*., 2004]. Thus, LULCC should be carefully considered in future climate projections.

Similar to *Osborne et al*. [2004] and *Notaro et al*. [2011], our study shows that the LULCC-induced response is strongly seasonal, as characterized by the most significant change in the monsoon transition season compared with the summer and winter monsoon seasons. The influence of the LULCC on the regional circulation is related to the LULCC-induced changes in the land surface albedo, land surface roughness, sensible heat flux, and latent heat flux. As summarized in Figure 10, the impact of the LULCC on the regional circulation could be enhanced by two positive feedbacks when the background circulation is weak during the monsoon transition seasons: (1) the temperature-subsidence-moisture feedback in the atmosphere and (2) the precipitation-soil moisture-evapotranspiration/albedo feedback between the land and atmosphere. The changes in soil moisture and sensible and latent heat fluxes that result from LULCC rarely propagate into the atmosphere in a significant way in June-July-August [*Findell et al*., 2009]. Based on our study, this insignificant propagation is likely due to the strong summer monsoon circulation, which dampens the influence of the LULCC on the atmosphere. Our study suggests that the impact of the LULCC on the regional climate depends not only on the land surface climate background, such as snow cover [*Pitman et al*., 2011], but also on the background circulation.

LULCC also results in detectable changes in the T2m variability over India and over the north China–east Mongolia region. In autumn, the LULCC causes an eastward extension of the dry-to-wet transition zone in northern India, where the variability in T2m is enhanced due to the strengthening land-atmosphere coupling. In winter, LULCC leads to enhanced T2m variability in India and reduces T2m variability in the NCEM region. Both changes are likely related to changes in the variability of the vertically integrated precipitable water (VIPW). A decrease in the VIPW results in reduced downward longwave radiation, which decreases the land surface temperature, and vice versa. In autumn, in addition to the change in the VIPW variability, the changes in the climatological mean meridional temperature gradient could also account for the changes in the T2m variability in the NCEM region. Thus, the changes in the T2m variability are caused by different mechanisms in different regions. In autumn and winter, the changes in T2m variability in the NCEM region likely results from the changes in the atmospheric variability. However, the T2m variability in India is likely linked to the changes in the land-atmosphere coupling strength.

It should be reiterated that the results reported in this study are based on two numerical experiments with potential and current land cover types using a single Earth system model (CESM). Because the CESM climatology exhibits significant systematic biases in monsoon circulation and precipitation, their response to LULCC and related conclusions may be CESM specific. The LULCC-induced changes in the monsoon circulation and precipitation do not reach the field significance level of 0.05. Thus, we suggest that multimodel and multiscenarios ensemble simulations would further help validate the effects of LULCC on monsoon Asia climate and the related mechanisms presented in this study [cf. *de Noblet-Ducoudré et al*., 2012]. In addition, it is still not very clear to what extent the air-sea coupling effect modulates the response of the Asian climate to LULCC. This interaction is of interests and warrants further investigation. The biogeochemical impact of LULCC on the concentration of $CO_2$ is also an important feedback to climate [*Eliseev and Mokhov*, 2011b], which remains to be quantified.

**Acknowledgments**
This research is supported jointly by the "National Basic Research Program of China" project 2011CB952004 and 2012CB956203, National Natural Science Foundation of China General Program (grants 40905042 and 41105039), and Carbon Budget and Relevant Issues of the Chinese Academy of Sciences (grant XDA05090207). NCEP-NCAR reanalysis 2 data and CMAP precipitation data are provided by the NOAA/OAR/ESRL PSD, Boulder, Colorado, USA, from their website at http://www.esrl.noaa.gov/psd/. We thank Michael Notaro and two anonymous reviewers for their insightful and helpful comments.

## References

Abe, M., A. Kitoh, and T. Yasunari (2003), An evolution of the Asian summer monsoon associated with mountain uplift—Simulation with the MRI atmosphere-ocean coupled GCM, *J. Meteorol. Soc. Jpn.*, *81*(5), 909–933.

Avila, F. B., A. J. Pitman, M. G. Donat, L. V. Alexander, and G. Abramowitz (2012), Climate model simulated changes in temperature extremes due to land cover change, *J. Geophys. Res.*, *117*, D04108, doi:10.1029/2011JD016382.

Bitz, C. M., M. Holland, M. Eby, and A. J. Weaver (2001), Simulating the ice-thickness distribution in a coupled climate model, *J. Geophys. Res.*, *106*, 2441–2463, doi:10.1029/1999JC000113.

Boisier, J. P., N. de Noblet-Ducoudré, A. J. Pitman, F. T. Cruz, C. Delire, B. J. J. M. vanden Hurk, M. K. van der Molen, C. Müller, and A. Voldoire (2012), Attributing the impacts of land-cover changes in temperate regions on surface temperature and heat fluxes to specific causes: Results from the first LUCID set of simulations, *J. Geophys. Res.*, *17*, D12116, doi:10.1029/2011JD017106.

Chang, C. P., and K. M. Lau (1980), Northeasterly cold surges and near-equatorial disturbances over the winter MONEX area during December 1974. Part II: Planetary-scale aspects, *Mon. Weather Rev.*, *108*, 298–312.

Chen, X., M. Lei, and J.-P. Tang (2006), Simulating the effect of changed vegetation on the climate change in Eurasia [in Chinese], *Adv. Earth Sci.*, *21*(10), 1075–1082.

Cui, X. F., H.-F. Graf, B. Langmann, W. Chen, and R. H. Huang (2006), Climate impacts of anthropogenic land use changes on the Tibetan Plateau, *Global Planet. Change*, *54*, 33–56.

Dai, Y., et al. (2003), The common land model, *Bull. Am. Meteorol. Soc.*, *84*, 1013–1023.

Davin, E. L., and N. de Noblet-Ducoudré (2010), Climatic impact of global-scale deforestation: Radiative versus nonradiative processes, *J. Clim.*, *23*, 97–112.

de Noblet-Ducoudré, N., et al. (2012), Determining robust impacts of land-use induced land-cover changes on surface climate over North America and Eurasia: Results from the first of LUCID experiments, *J. Clim.*, *25*, 3261–3281.

Delire, C., P. Behling, M. Coe, J. Foley, R. Jacob, J. Kutzbach, Z. Liu, and S. Vavrus (2001), Simulated response of the atmosphere-ocean system to deforestation in the Indonesian Archipelago, *Geophys. Res. Lett.*, *28*, 2081–2084, doi:10.1029/2000GL011947.

Ding, Y., Q. Li, and W. Dong (2005), A numerical simulation study of the impacts of vegetation changes on regional climate in China [in Chinese], *Acta Meteorol. Sin.*, *63*(5), 613–621.

Douglas, E. M., D. Niyogi, S. Frolking, J. B. Yeluripati Sr., R. A. Pielke, C. J. Vörösmarty, and U. C. Mohanty (2006), Changes in moisture and energy fluxes due to agricultural land use and irrigation in the Indian Monsoon Belt, *Geophys. Res. Lett.*, *33*, L14403, doi:10.1029/2006GL026550.

Douglas, E. M., A. Beltrán-Przekurat, D. Niyogi Sr., R. A. Pielke, and C. J. Vörösmarty (2009), The impact of agricultural intensification and irrigation on land–atmosphere interactions and Indian monsoon precipitation—A mesoscale modeling perspective, *Global Planet. Change*, *67*, 117–128.

Easterling, D. R., et al. (1997), Maximum and minimum temperature trends for the globe, *Science*, *277*, 364–367.

Eliseev, A. V., and I. I. Mokhov (2011a), Effect of including land use driven radiative forcing of the surface albedo of land on climate response in the 16th–21st centuries, *Izv. Atmos. Oceanic Phys.*, *47*(1), 15–30, doi:10.1134/S0001433811010075.

Eliseev, A. V., and I. I. Mokhov (2011b), Uncertainty of climate response to natural and anthropogenic-forcings due to different land use scenarios, *Adv. Atmos. Sci.*, *28*(5), 1215–1232, doi:10.1007/s00376-010-0054-8.

Elmore, K. L., M. E. Baldwin, and D. M. Schultz (2006), Field significance revisited: Spatial bias errors in forecasts as applied to the Eta model, *Mon. Weather Rev.*, *134*(2), 519–531.

Findell, K. L., A. J. Pitman, M. H. England, and P. J. Pegion (2009), Regional and global impacts of land cover change and sea surface temperature anomalies, *J. Clim.*, *22*, 3248–3268.

Fu, C. (2003), Potential impacts of human-induced land cover change on East Asia monsoon, *Global Planet. Change*, *37*, 219–229.

Gao, X., Y. Luo, W. Lin, Z. Zongci, and F. Giorgi (2003), Simulation of effects of land use change on climate in China by a regional climate model, *Adv. Atmos. Sci.*, *20*(4), 583–592.

Gent, P. R., et al. (2011), The Community Climate System Model version 4 (CCSM4), *J. Clim.*, *24*, 4973–4991.

Goldewijk, K. K. (2001), Estimating global land use change over the past 300 years: The HYDE database, *Global Planet. Change*, *15*(2), 417–433.

Harris, I., P. D. Jones, T. J. Osborn, and D. H. Lister (2014), Updated high-resolution grids of monthly climatic observations—The CRU TS3.10 dataset, *Int. J. Climatol.*, *34*, 623–642.

Kalnay, E., and M. Cai (2003), Impact of urbanization and land-use change on climate, *Nature*, *423*, 528–531.

Kalnay, E., et al. (1996), The NCEP/NCAR 40-year reanalysis project, *Bull. Am. Meteorol. Soc.*, *77*, 437–471.

Kantha, L. H., and C. A. Clayson (2000), *Numerical Models of Oceans and Oceanic Process*, pp. 324–327, Academic Press, San Diego, Calif.

Karl, T. R., P. D. Jones, R. W. Knight, G. Kukla, N. Plummer, V. Razuvayev, K. P. Gallo, J. Lindseay, R. J. Charlson, and T. C. Peterson (1993), A new perspective on recent global warming: Asymmetric trends on daily maximum and minimum temperature, *Bull. Am. Meteorol. Soc.*, *74*, 1007–1023.

Kioth, A. (2004), Effects of mountain uplift on East Asian summer climate investigated by a coupled atmosphere-ocean GCM, *J. Clim.*, *17*, 783–802.

Koster, R. D., et al. (2004), Regions of strong coupling between soil moisture and precipitation, *Science*, *305*, 1138–1140.

Koster, R. D., et al. (2006), GLACE: The global land-atmosphere coupling experiment. Part I. Overview, *J. Hydrometeorol.*, *7*, 590–610.

Lawrence, P. J., and T. N. Chase (2010), Investigating the climate impacts of global land cover change in the community climate system model, *Int. J. Climatol.*, doi:10.1002/joc.2061.

Lawrence, D. M., et al. (2011), Parameterization improvements and functional and structural advances in version 4 of the Community Land Model, *J. Adv. Model. Earth Syst.*, *3*, M03001, doi:10.1029/2011MS000045.

Lee, S.-Y., H.-J. Shin, and C. Wang (2013), Nonlinear effects of coexisting surface and atmospheric forcing of anthropogenic absorbing aerosols: Impact on the South Asian monsoon onset, *J. Clim.*, *26*, 5594–5607.

Li, L., H. Zhang, B. Hu, G.-R. Liu, Z.-R. Liu, and Y.-S. Wang (2012), Characteristics of soil heat flux in different soil types in China [in Chinese], *Plateau Meteorol.*, *3*(2), 322–328.

Li, Q., and Y. Wang (2012), Changes in the observed trends in extreme temperatures over China around 1990, *J. Clim.*, *25*, 5208–5222.

Lin, S. J. (2004), A"vertically Lagrangian" finite-volume dynamical core for global models, *Mon. Weather Rev.*, *132*, 2293–2307.

Lipscomb, W. H. (2001), Remapping the thickness distribution in sea ice models, *J. Geophys. Res.*, *106*, 13,989–14,000, doi:10.1029/2000JC000518.

Livezey, R. E., and W. Y. Chen (1983), Statistical field significance and its determination by Monte Carlo Techniques, *Mon. Weather Rev.*, *111*, 46–59.

Lv, S., and Y. Chen (1999), The influence of northwest China afforestation on regional climate in China, *Plateau Meteorol.*, *18*(3), 416–424.

Ma, D., M. Notaro, Z. Liu, G. Chen, and Y. Liu (2012), Simulated impacts of afforestation in East China monsoon region as modulated by ocean variability, *Clim. Dyn.*, *41*, 2439–2450.
Mahmood, R., K. G. Hubbard, and C. Carlson (2004), Modification of growing season surface temperature records in the Northern Great Plains due to land use transformation: Verification of modeling results and implication for global climate change, *Int. J. Climatol.*, *24*, 311–327.
Meehl, G. A., J. M. Arblaster, D. M. Lawrence, A. Seth, E. K. Schneider, B. P. Kirtman, and D. Min (2006), Monsoon regimes in the CCSM3, *J. Clim.*, *19*, 2482–2495.
Meehl, G. A., J. M. Arblaster, J. M. Caron, H. Annamalai, M. Jochum, A. Chakraborty, and R. Murtugudde (2012), Monsoon regimes and processes in CCSM4. Part I: The Asian-Australian monsoon, *J. Clim.*, *25*, 2583–2608.
Myhre, G., et al. (2013), Anthropogenic and natural radiative forcing, in *Climate Change 2013: The Physical Science Basis. Contribution of Working Group I to the Fifth Assessment Report of the Intergovernmental Panel on Climate Change*, edited by T. F. Stocker et al., 1535 pp., Cambridge Univ. Press, Cambridge, U. K., and New York.
Notaro, M., G. Chen, and Z. Liu (2011), Vegetation feedbacks to climate in the global monsoon regions, *J. Clim.*, *24*, 5740–5756.
Oke, T. R. (1987), *Boundary Layer Climates*, 2nd ed, 435 pp., Routledge, New York.
Osborne, T. M., D. M. Lawrence, J. M. Slingo, A. J. Challinor, and T. R. Wheeler (2004), Influence of vegetation on the local climate and hydrology in the tropics: Sensitivity to soil parameters, *Clim. Dyn.*, *23*, 45–61.
Pitman, A. J., et al. (2009), Uncertainties in climate responses to past land cover change: First results from the LUCID intercomparison study, *Geophys. Res. Lett.*, *36*, L14814, doi:10.1029/2009GL039076.
Pitman, A. J., F. B. Avila, G. Abramowitz, Y. P. Wang, S. J. Phipps, and N. de Noblet-Ducoudré (2011), Importance of background climate in determining impact of land-cover change on regional climate, *Nat. Clim. Change*, *1*, 472–475.
Pitman, A. J., et al. (2012), Effects of land cover change on temperature and rainfall extremes in multi-model ensemble simulations, *Earth Syst. Dyn.*, *3*(2), 213–231, doi:10.5194/esd-3-213-2012.
Ramankutty, N., and J. A. Foley (1999), Estimating historical changes in global land cover: Croplands from 1700 to 1992, *Global Biogeochem. Cycles*, *13*(4), 997–1027, doi:10.1029/1999GB900046.
Rosenberg, N. J., B. L. Blad, and S. B. Verma (1983), *Microclimate: The Biological Environment*, 583 pp., Wiley, New York.
Sen Roy S., R. Mahmood, D. Niyogi, M. Lei, S. A. Foster, K. G. Hubbard, E. Douglas, and R. A. Pielke Sr. (2007), Impacts of the agricultural Green Revolution–induced land use changes on air temperatures in India, *J. Geophys. Res.*, *112*, D21108, doi:10.1029/2007JD008834.
Sen Roy, S., R. Mahmood, A. I. Quintanar, and A. Gonzalez (2011), Impacts of irrigation on dry season precipitation in India, *Theor. Appl. Climatol.*, *104*, 193–207, doi:10.1007/s00704-010-0338-z.
Seneviratne, S. I., D. Lüthi, M. Litschi, and C. Schär (2006), Land-atmosphere coupling and climate change in Europe, *Nature*, *443*, 205–209.
Seneviratne, S. I., T. Corti, E. L. Davin, M. Hirschi, E. B. Jaeger, I. Lehner, B. Orlowsky, and A. J. Teuling (2010), Investigating soil moisture-climate interactions in a changing climate: A review, *Earth Sci. Rev.*, *99*, 125–161.
Shiu, C.-J., S. Liu, and J.-P. Chen (2009), Diurnally asymmetric trends of temperature, humidity, and precipitation in Taiwan, *J. Clim.*, *22*, 5635–5649.
Smith, R. D., et al. (2010), The Parallel Ocean Program (POP) reference manual, Los Alamos National Laboratory, Tech. Rep. LAUR-10-01853, 140 pp.
Stone, D. A., and A. J. Weaver (2002), Daily maximum and minimum temperature trends in a climate model, *Geophys. Res. Lett.*, *29*(9), 1356, doi:10.1029/2001/GL014556.
Sud, Y. C., and W. E. Smith (1985), Influence of local land-surface processes on the Indian monsoon: A numerical study, *J. Clim. Appl. Meteorol.*, *24*, 1015–1036.
Takata, K., K. Saito, and T. Yasunari (2009), Changes in the Asian monsoon climate during 1700–1850 induced by preindustrial cultivation, *Proc. Natl. Acad. Sci. U.S.A.*, *106*(24), 9586–9589.
United Nations (2013), *World Population Prospects: The 2012 Revision*, vol. 1, Comprehensive Tables, 439 pp., United Nations Department of Economic and Social Affairs (UN DESA) Population Division, New York.
Wohlfahrt, J., S. P. Harrison, and P. Braconnot (2004), Synergistic feedbacks between ocean and vegetation on mid- and high-latitude climates during the mid-Holocene, *Clim. Dyn.*, *22*, 223–238.
Yang, Z.-L., Y. Dai, R. E. Dickinson, and W. J. Shuttleworth (1999), Sensitivity of ground heat flux to vegetation cover fraction and leaf area index, *J. Geophys. Res.*, *104*, 19,505–19,514, doi:10.1029/1999JD900230.
Zhang, H., and X. Gao (2009), On the atmospheric dynamical responses to land-use change in East Asian monsoon region, *Clim. Dyn.*, *33*, 409–426.
Zhang, Y.-C. (2004), Virtual numerical experiments on the climatic effects of vegetation type changes over northern China [in Chinese], *J. Nanjing Univ. Nat. Sci. Edn.*, *40*(6), 684–691.
Zheng, Y., Y. Qian, M. Miao, G. Yu, Y. Kong, and D. Zhang (2002a), The effects of vegetation change on regional climate. I: Simulation results, *Acta Meteorol. Sin.*, *60*(1), 1–16.
Zheng, Y., Y. Qian, M. Miao, G. Yu, Y. Kong, and D. Zhang (2002b), The effects of vegetation change on regional climate. II: Mechanisms, *Acta Meteorol. Sin.*, *60*(1), 17–30.
Zhou, L., R. E. Dickinson, Y. Tian, R. Vose, and Y. Dai (2007), Impact of vegetation removal and soil aridation on diurnal temperature range in a semiarid region—Application to the Sahel, *Proc. Natl. Acad. Sci. U.S.A.*, *104*(46), 17,937–17,942.
Zhou, L., R. E. Dickinson, A. G. Dai, and P. Dirmeyer (2010), Detection and attribution of anthropogenic forcing to diurnal temperature range changes from 1950 to 1999: Comparing multi-model simulations with observations, *Clim. Dyn.*, *35*, 1289–1307.
Zwiers, F., and H. von Storch (1995), Taking serial correlation into account in tests of the mean, *J. Clim.*, *8*, 336–351.